CrossMark

TOI-561 b: A Low-density Ultra-short-period "Rocky" Planet around a Metal-poor Star

Casey L. Brinkman[1], Lauren M. Weiss[2], Fei Dai[3], Daniel Huber[1], Edwin S. Kite[4], Diana Valencia[5],
Jacob L. Bean[6], Corey Beard[7], Aida Behmard[8], Sarah Blunt[8], Madison Brady[6], Benjamin Fulton[9],
Steven Giacalone[10], Andrew W. Howard[8], Howard Isaacson[10,11], David Kasper[6], Jack Lubin[7], Mason MacDougall[12],
Joseph M. Akana Murphy[13], Mykhaylo Plotnykov[5], Alex S. Polanski[14], Malena Rice[15,16,19], Andreas Seifahrt[6],
Guðmundur Stefánsson[17,20], and Julian Stürmer[18]
[1] Institute for Astronomy, University of Hawaiʻi, 2680 Woodlawn Drive, Honolulu, HI 96822 USA; clbrinkm@hawaii.edu
[2] Department of Physics and Astronomy, University of Notre Dame, Notre Dame, IN 46556, USA
[3] Division of Geological and Planetary Sciences, 1200 E. California Boulevard, Pasadena, CA 91125, USA
[4] Department of the Geophysical Sciences, University of Chicago, Chicago, IL 60637, USA
[5] Centre for Planetary Sciences, University of Toronto, 1265 Military Trail, Toronto, ON M1C 1A4, Canada
[6] Department of Astronomy & Astrophysics, University of Chicago, 5640 S. Ellis Avenue, Chicago, IL 60637, USA
[7] Department of Physics & Astronomy, University of California Irvine, Irvine, CA 92697, USA
[8] Department of Astronomy, California Institute of Technology, Pasadena, CA 91125, USA
[9] NASA Exoplanet Science Institute/Caltech-IPAC, MC 314-6, 1200 E. California Boulevard, Pasadena, CA 91125, USA
[10] Department of Astronomy, 501 Campbell Hall, University of California, Berkeley, CA 94720, USA
[11] Centre for Astrophysics, University of Southern Queensland, Toowoomba, QLD, Australia
[12] Astronomy Department, 475 Portola Plaza, University of California, Los Angeles, CA 90095, USA
[13] Department of Astronomy and Astrophysics, University of California, Santa Cruz, CA 95064, USA
[14] Department of Physics and Astronomy, University of Kansas, Lawrence, KS 66045, USA
[15] Department of Physics and Kavli Institute for Astrophysics and Space Research, Massachusetts Institute of Technology, Cambridge, MA 02139, USA
[16] Department of Astronomy, Yale University, New Haven, CT 06511, USA
[17] Department of Astrophysical Sciences, Princeton University, 4 Ivy Lane, Princeton, NJ 08540, USA
[18] Landessternwarte, Zentrum für Astronomie der Universität Heidelberg, Königstuhl 12, D-69117 Heidelberg, Germany

Abstract

TOI-561 is a galactic thick-disk star hosting an ultra-short-period (0.45-day-orbit) planet with a radius of 1.37 $R_\oplus$, making it one of the most metal-poor ([Fe/H] = −0.41) and oldest (≈10 Gyr) sites where an Earth-sized planet has been found. We present new simultaneous radial velocity (RV) measurements from Gemini-N/MAROON-X and Keck/HIRES, which we combined with literature RVs to derive a mass of $M_b = 2.24 \pm 0.20\,M_\oplus$. We also used two new sectors of TESS photometry to improve the radius determination, finding $R_b = 1.37 \pm 0.04\,R_\oplus$ and confirming that TOI-561 b is one of the lowest-density super-Earths measured to date ($\rho_b = 4.8 \pm 0.5\,\mathrm{g\,cm^{-3}}$). This density is consistent with an iron-poor rocky composition reflective of the host star's iron and rock-building element abundances; however, it is also consistent with a low-density planet with a volatile envelope. The equilibrium temperature of the planet (∼2300 K) suggests that this envelope would likely be composed of high mean molecular weight species, such as water vapor, carbon dioxide, or silicate vapor, and is likely not primordial. We also demonstrate that the composition determination is sensitive to the choice of stellar parameters and that further measurements are needed to determine whether TOI-561 b is a bare rocky planet, a rocky planet with an optically thin atmosphere, or a rare example of a nonprimordial envelope on a planet with a radius smaller than 1.5 $R_\oplus$.

Unified Astronomy Thesaurus concepts: Exoplanets (498); Extrasolar rocky planets (511); Super Earths (1655); Exoplanet surface composition (2022); Exoplanet atmospheric composition (2021)

Supporting material: machine-readable table

1. Introduction

TOI-561 b is a rare ultra-short-period (USP; $P = 0.45$ days) planet orbiting a star that originated in the galactic thick disk (Lacedelli et al. 2021; Weiss et al. 2021). It was the first chemically and kinematically confirmed thick-disk exoplanetary system detected by TESS, and it is the first USP discovered around a thick-disk star (Weiss et al. 2021). At 1.4 times Earth's radius, TOI-561 b is a super-Earth-size planet, and the TOI-561 system is one of only two confirmed planetary systems discovered around thick-disk stars to date (the other is Kepler-444; Campante et al. 2015).[21] TOI-561 is 10 ± 3 Gyr old (Weiss et al. 2021), making TOI-561 b one of the oldest known super-Earth-sized planets, indicating that rocky planets have been forming for nearly the age of the universe, even in metal-poor environments. Previous studies of this system suggest an even more unique aspect of this planet: it is the lowest-density super-Earth discovered to date, and potentially inconsistent with having a rocky planet composition (Lacedelli et al. 2021, 2022).

[19] 51 Pegasi b Fellow.
[20] Henry Norris Russell Fellow.

[21] Additional planets have been validated around thick-disk stars but not confirmed with RV mass measurements, such as LHS 1518b (Gan et al. 2020).

Two groups have previously published mass and radius measurements for TOI-561 b, along with the three additional sub-Neptune-sized planets in the system. Weiss et al. (2021) used radial velocities (RVs) from the Keck/HIRES spectrograph and found a mass of $M_b = 3.24 \pm 0.83\ M_\oplus$, a radius of $R_b = 1.45 \pm 0.11\ R_\oplus$, and a density of $\rho_b = 5.6 \pm 2.2\ \mathrm{g\,cm}^{-3}$. This is approximately one standard deviation less dense than a planet with an Earth-like composition would be at $R_b = 1.45\ R_\oplus$. Lacedelli et al. (2021) used RVs from the TNG/HARPS-N spectrograph and found an even lower mass of $M_b = 1.59 \pm 0.36\ M_\oplus$, a radius of $R_b = 1.43 \pm 0.11\ R_\oplus$, and a corresponding density of $\rho_b = 3.0 \pm 0.8\ \mathrm{g\,cm}^{-3}$. More recently, Lacedelli et al. (2022) combined the literature RVs from HIRES and HARPS-N with new HARPS-N RVs, finding a mass of $M_b = 2.00 \pm 0.23$ and a density of $\rho_b = 3.8 \pm 0.5\ \mathrm{g\,cm}^{-3}$. Based on their analysis, TOI-561 b is inconsistent with a rocky composition and was suggested to have a water steam envelope.

From the solar system, we expect large planets to have extensive low molecular weight envelopes, while smaller planets are composed primarily of rock and metal. The masses and radii of small exoplanets suggest a transition between primarily rocky and gas-enveloped planets at approximately $1.5\ R_\oplus$ (Weiss & Marcy 2014; Rogers 2015; Fulton et al. 2017), with planets smaller than $1.5\ R_\oplus$ often having compositions consistent with Earth-like iron-to-silicate ratios (Dressing et al. 2015). However, existing super-Earth-mass measurements indicate a wide diversity of densities among those planets with $R > 1.5\ R_\oplus$—far more diverse than we observe for rocky planets in our own solar system (Marcy et al. 2014; Morton et al. 2016; Dai et al. 2019). These densities suggest that the interior compositions of Earth- and super-Earth-sized planets could potentially vary from entirely made of silicate rock to predominantly made of iron (Bonomo et al. 2019), with high molecular mass atmospheres possible (Angelo & Hu 2017; Kite & Schaefer 2021).

Because exoplanets are born from the same primordial nebular material as their host star, the abundances of refractory elements in planets should correlate with those of their host star, and stellar abundances can be used as a prior for rocky planet chemical composition (Dorn et al. 2015). Comparing the population of rocky exoplanets to the population of host stars, we see that planets span a wider range in refractory abundances than stars (Plotnykov & Valencia 2020). When looking at one-to-one comparisons of rocky exoplanets and their host stars, the error bars—especially in mass—are too large in most cases to draw definite conclusions (Plotnykov & Valencia 2020; Schulze et al. 2021), except for a few cases where planets differ in composition by 1σ compared to their star (Schulze et al. 2021). However, when performing one-to-one comparisons, there appears to be a correlation between stellar and planet enrichment (Adibekyan et al. 2021). Improving the mass and radius estimates on TOI-561 b provides a unique opportunity to compare the planetary and stellar compositional similarities for such an old, highly irradiated planet.

In this paper, we further refine the radius and mass measurements for TOI-561 b, along with our understanding of its bulk composition. We first use two additional sectors of TESS photometry to measure the radius of the planet. We then present the results of the first simultaneous RV program combining MAROON-X (Seifahrt et al. 2018, 2020), a new fiber-fed RV spectrometer on Gemini-N, and HIRES, a well-characterized spectrometer on Keck I, to measure the mass of the planet in combination with literature RVs. We then combine these mass and radius measurements to investigate the potential compositions of TOI-561 b and the sensitivity of these results to stellar parameter choice and assumptions about the mantle melt fraction.

2. Planet Radii

The TESS spacecraft has observed TOI-561 in Sectors 8, 35, 45, and 46. Weiss et al. (2021) and Lacedelli et al. (2021) used Sector 8, while Lacedelli et al. (2022) used Sectors 8 and 35. We used all four available sectors, analyzing both TESS's typical 2 minute cadence and 20 s cadence light curves for Sectors 45 and 46. The addition of 20 s data is particularly valuable, since it has shown to yield improved photometric precision for bright stars (Huber et al. 2022).

To improve the constraints on the planet radii, we downloaded the simple aperture photometry (SAP) light curves of relevant TESS sectors from the Mikulski Archive for Space Telescopes (MAST) at the Space Telescope Science Institute. The specific observations analyzed can be accessed via 10.17909/7y1e-1k46. Sector 8 photometry featured two transits that Weiss et al. (2021) interpreted as two transits of the same planet at 16.287 ± 0.005 days (giving a total of three transiting planets for the system), while Lacedelli et al. (2021) interpreted it as single transits of two different planets (giving four transiting planets). Follow-up photometry from CHEOPS lifts this degeneracy in favor of the four-planet model, with planet d at an orbital period of 25.7124 ± 0.0002 days and planet e at a period of 77.03 ± 0.25 days (Lacedelli et al. 2022). The additional TESS observations of Sectors 45 and 46 further support the four-planet model as described in Lacedelli et al. (2022).

Our analysis employs the Python package Batman (Kreidberg 2015) to model the transit light curves. We imposed a Gaussian prior on the host star mean density of 1.38 ± 0.11 $\rho_\odot$ (Weiss et al. 2021). The mean stellar density is a global parameter that is used to generate the transit light curves of all planets in the TOI-561 system consistently (Seager & Mallen-Ornelas 2003). Two other global parameters are the quadratic limb-darkening coefficients $q1$ and $q2$ as parameterized by Kipping (2013). Assuming circular orbits, each planet also has the following transit parameters: the orbital period P_{orb}, the time of conjunction T_c, the planet-to-star radius ratio $R_p/R_\star$, and the impact parameter $b \equiv a \cos i/R_\star$. The semimajor axis in units of stellar radii $a/R_\star$ is implicitly constrained based on the orbital periods and the host star density.

For each planet, we started from the transit parameters reported by the TESS team on ExoFOP.[22] We isolated the individual transit with a window size of 2 times the reported transit duration. After removing any overlapping transits, we analyzed 193, 8, 4, and 2 individual transits for planets b, c, d, and e, respectively. In our final global fit, we analyzed all transits simultaneously. We treated any overlapping transits as a simple sum of the individual transit light curves (i.e., ignoring any possible planet–planet eclipse). We fitted and removed any local stellar variability with a quadratic polynomial. We then fit all transits of each planet together with the Levenberg–Marquardt optimization in Python package lmfit (Newville et al. 2014). The best-fit model then served as a new template

---

[22] https://exofop.ipac.caltech.edu

Table 1
TOI-561 b Transit Fit

Transit Parameter	Posterior Results
$\rho_\star$ $(\rho_\odot)$	1.29 ± 0.04
q_1	0.34 ± 0.20
q_2	0.32 ± 0.22
$r_p/r_\star$	0.01507 ± 0.00043
$i_{\rm orb}(^\circ)$	87.9 ± 1.8
$a/R_\star$	2.669 ± 0.034
b	0.10 ± 0.08
e	0 (fixed)
ω	0 (fixed)
$P_{\rm orb}$ (days)	0.4465690 ± 0.0000012
T_c (BJD $-2,457,000$)	1517.4984 ± 0.0019

Note. Transit parameters of TOI-561 b based on sectors 8 and 35 (2 minute cadence) and sectors 45 and 46 (both 2 minute and 20 s cadence available). Values were found using Batman.

transit model to fit the individual transit and local stellar variability. We repeated this process three times. We did not detect any quasi-sinusoidal variation in the individual transit times that would hint at transit timing variations.

Finally, we sampled the posterior distribution of a global transit model with the affine-invariant Markov Chain Monte Carlo (MCMC) method using the Python package emcee (Foreman-Mackey et al. 2013). We initialized 128 walkers near the best-fit Levenberg–Marquardt solution found by lmfit. We ran the code for 50,000 links, after which we checked for convergence by calculating the autocorrelation lengths for each parameter, which range from 30 to 200 samples. For even the slowest converging parameter (200 samples), we are using more than $250\times$ more samples than the autocorrelation length, making convergence a safe assumption[23] (Foreman-Mackey et al. 2013).

The transit parameters from our posterior for TOI-561 b are summarized in Table 1, while the orbital periods and times of conjunction of all four planets are used to further model the RV measurements (Section 3). Crucially, the planet/star radius ratio of planet b was constrained to be 0.01507 ± 0.00043. Using the stellar radius from Weiss et al. (2021), this translates to a planet radius of $R_b = 1.37 \pm 0.04$ $R_\oplus$. The phase-folded transit for TOI-561 b using our best-fit model is shown in Figure 1.

We additionally analyzed the TESS PDCSAP data to look for any potential variations in the transit depth between TESS sectors using the exoplanet package (Foreman-Mackey et al. 2021) and its dependencies (Agol et al. 2020; Kumar et al. 2019; Astropy Collaboration et al. 2013, 2018; Kipping 2013; Luger et al. 2019; Salvatier et al. 2016; Theano Development Team 2016). We downloaded the TESS Pre-search Data Conditioning SAP (PDCSAP) flux photometry using Light-kurve (Lightkurve Collaboration et al. 2018) and masked the transits of planets c, d, and e. We then imposed a Gaussian prior on stellar density (same as above) and used Gaussian priors on period and conjunction time for TOI-561 b using the values and uncertainties reported in Lacedelli et al. (2022). We then created a transit model using limb-darkening parameters from Kipping (2013) (also described above). We then ran a Hamiltonian Monte Carlo using PyMC3 (Salvatier et al. 2016)

to sample the posterior distribution using 20 chains and 10,000 draws and checked for convergence by ensuring that the number of draws is >50 times greater than the longest autocorrelation length.

We fit each sector of data, and each available cadence, individually and combined to see the variation in transit depth between sectors and observation cadence (Table 2). The sectors with the largest difference in R_P/R_* (Sector 8, 2 minute cadence, and Sector 46, 20 s cadence) differ by 2σ. The combined fits from all sectors and cadences agree with the R_P/R_* found using Batman. The values for transit depth reported are from Batman.

3. Planet Masses

3.1. HIRES RVs

Our analysis incorporates 102 total RVs from the High Resolution Echelle Spectrograph (HIRES) on the W. M. Keck Observatory 10 m telescope Keck I on Maunakea, Hawai'i (Vogt et al. 1994). Weiss et al. (2021) obtained 60 RVs between 2019 May and 2020 October through the TESS-Keck Survey (TKS) collaboration (Chontos et al. 2021). We collected 42 additional RVs from 2020 October to 2022 March.[24] The RVs used in this paper are listed in Table 3.

We used the standard California Planet Search (CPS) data reduction pipeline as described in Howard et al. (2010). This method uses an iodine cell mounted in front of the slit in order to provide a provide a wavelength reference (Marcy & Butler 1992). Sky subtraction was performed as part of the raw reduction through the use of a $14.''0$-long slit in order to spatially resolve the sky with respect to the seeing-limited point-spread function (PSF; FWHM $\approx 1.''0$). Measuring the RVs requires characterizing the PSF of the spectrometer, which is time variable owing primarily to changing seeing and weather. The CPS Doppler routine involves forward-modeling the iodine-imprinted spectrum of a star as the combination of a library iodine spectrum and a velocity-shifted, iodine-free, PSF-deconvolved template spectrum of the target star, the combination of which is then convolved with the best-fit PSF. To deconvolve the PSF from the iodine-free template, we observed rapidly rotating B stars with the iodine cell in the light path immediately before and after the template, effectively sampling the PSF at the time of the template in the iodine absorption profiles.

3.2. HARPS-North RVs

Our analysis also incorporates 143 published RVs from the HARPS-N spectrograph installed on the 3.6 m Telescopio Nazionale Galileo (TNG) at the Observatorio Roque de Los Muchachos in La Palma, Spain. Originally published in Lacedelli et al. (2021) and Lacedelli et al. (2022), these RVs were collected between 2019 November and 2021 June.

3.3. MAROON-X RVs

MAROON-X is a new, state-of-the-art fiber-fed spectrograph mounted on the 8.1 m Gemini North telescope on Maunakea, Hawai'i. It operates in the red–optical (500–920 nm) with resolving power $R \approx 85,000$ and uses both red and blue arms to get two RV measurements per exposure

---

[23] The suggested sample size to ensure convergence is $N > 50\tau$, where τ is the autocorrelation length.

[24] Telescope time was allocated by University of Hawaii, University of California, California Institute of Technology, and NASA.

Table 2
R_P/R_* Measured for Each Available Sector (8, 35, 45, 46) of TESS Photometry, and Where Available with Both 2 Minute and 20 s Cadence Data

Sector	8	35	45	46	Joint Fit
2 minute	0.0155 ± 0.0009	0.0149 ± 0.0011	0.0141 ± 0.0009	0.01460 ± 0.0009	0.0155 ± 0.0005
20 s	N/A	N/A	0.0147 ± 0.0008	0.01396 ± 0.0009	0.0145 ± 0.0007

(Seifahrt et al. 2016, 2018, 2020). MAROON-X has demonstrated a stability of $30\,\mathrm{cm\,s^{-1}}$ and has been used to measure some of the most precise masses for rocky planets in the literature to date (Trifonov et al. 2021; Winters et al. 2022).

Our observations used the simultaneous calibration fiber of MAROON-X, which allows for a robust order-by-order drift correction to submeter-per-second precision. The raw data were reduced using a custom pipeline based on that developed for CRIRES (Bean et al. 2010), and RVs were computed using SERVAL (Zechmeister et al. 2018). A full description of MAROON-X data reduction can be found in Winters et al. (2022).

We collected a total of 70 RVs between 2021 February and 2021 May, 35 individual exposures with RVs from the red and blue arms.[25] We used an integration time of 460 s, and we found that the blue-arm RVs had a median uncertainty of $1.4\,\mathrm{m\,s^{-1}}$, while those from the red arm had a median uncertainty of $2.8\,\mathrm{m\,s^{-1}}$.

We observed TOI-561 with a mixture of high-cadence runs and long-term monitoring. High-cadence observations (five or more RVs per night) allowed us to sample the full phase curve of 0.45-day-orbit planet TOI-561 b, while freezing out the contribution of longer-period planets. During our highest-cadence run, we collected five to six RVs per night for three nights in 2021 February (Figure 2). We also collected simultaneous observations on HIRES during this run to verify the stability of MAROON-X.

3.4. Keplerian Orbital Fit

We used the open-source Python package RadVel (Fulton et al. 2018) to model the RVs. We measured the mass of each planet by fitting the RVs for a Keplerian orbit, in which the RV curve is described by the orbital period (P), conjunction time (T_c), eccentricity (e), argument of periastron, and RV semiamplitude (K) of each planet. We include two additional terms per data set to fit the RVs: a zero-point offset (γ) and an RV jitter term (σ_j). Jitter accounts for additional Gaussian noise that can be astrophysical in origin or can come from systematics of the spectrograph. This additional uncertainty was added in quadrature with the intrinsic uncertainties on the RVs during our optimization of the likelihood function and MCMC analysis (described below).

Our constraints on period and conjunction time for TOI-561 b and c from TESS photometry are more precise than we would be able to measure using RVs; therefore, we fix these values to the photometric ones in the RV fit. As a test, we also fit the RVs with Gaussian priors on conjunction time and period centered on the best-fit values from TESS photometry, and we recover posterior values consistent with the solution using fixed period and conjunction time. We assume that the USP has a circular orbit (Weiss et al. 2021), and we also assume low-eccentricity orbits for the three outer planets, as is typical for compact multiplanet systems (Deck et al. 2013; Eylen et al. 2019;

---

[25] Telescope time was allocated by the University of Hawaii.

Table 3
TOI-561 RVs

Time (BJD)	RV ($\mathrm{m\,s^{-1}}$)	σ_{RV} ($\mathrm{m\,s^{-1}}$)	Spectrograph
2,459,267.750	−3.7	1.6	MAROON-X Blue
2,459,267.813	−5.3	1.4	MAROON-X Blue
2,459,267.750	−6.54	2.9	MAROON-X Red
2,459,267.813	−12.4	2.7	MAROON-X Red
2,459,632.851	−1.9	1.19	HIRES
2,459,649.771	0.1	1.5	HIRES

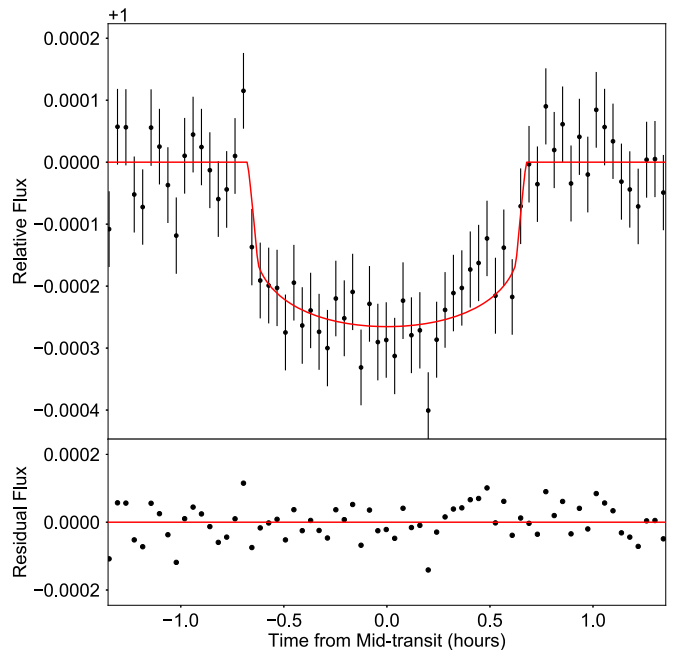(This table is available in its entirety in machine-readable form.)

Figure 1. Phase-folded TESS transit light curve of TOI-561 b from all available sectors. We have removed overlapping transits with other planets. We have binned the phased light curves (black). The red curve shows the best-fit transit model.

Mills et al. 2019; Yee et al. 2021). As a test, we used both models that allow the eccentricities to vary with no prior and models with eccentricity fixed at zero. The best-fit solution in either model prefers circular orbits, and as a consequence of the eight additional parameters, it produces a larger BIC for the model that allows variable eccentricity (1630 vs. 1580 with fixed circular orbits); therefore, we adopt eccentricities fixed at zero. Our model parameter constraints and posterior values are summarized in Table 4. After optimizing for the maximum likelihood fit, we ran RadVel's built-in MCMC algorithm (Foreman-Mackey et al. 2013) to explore the surrounding parameter space, estimate the uncertainty in the model parameters, and explore the covariance
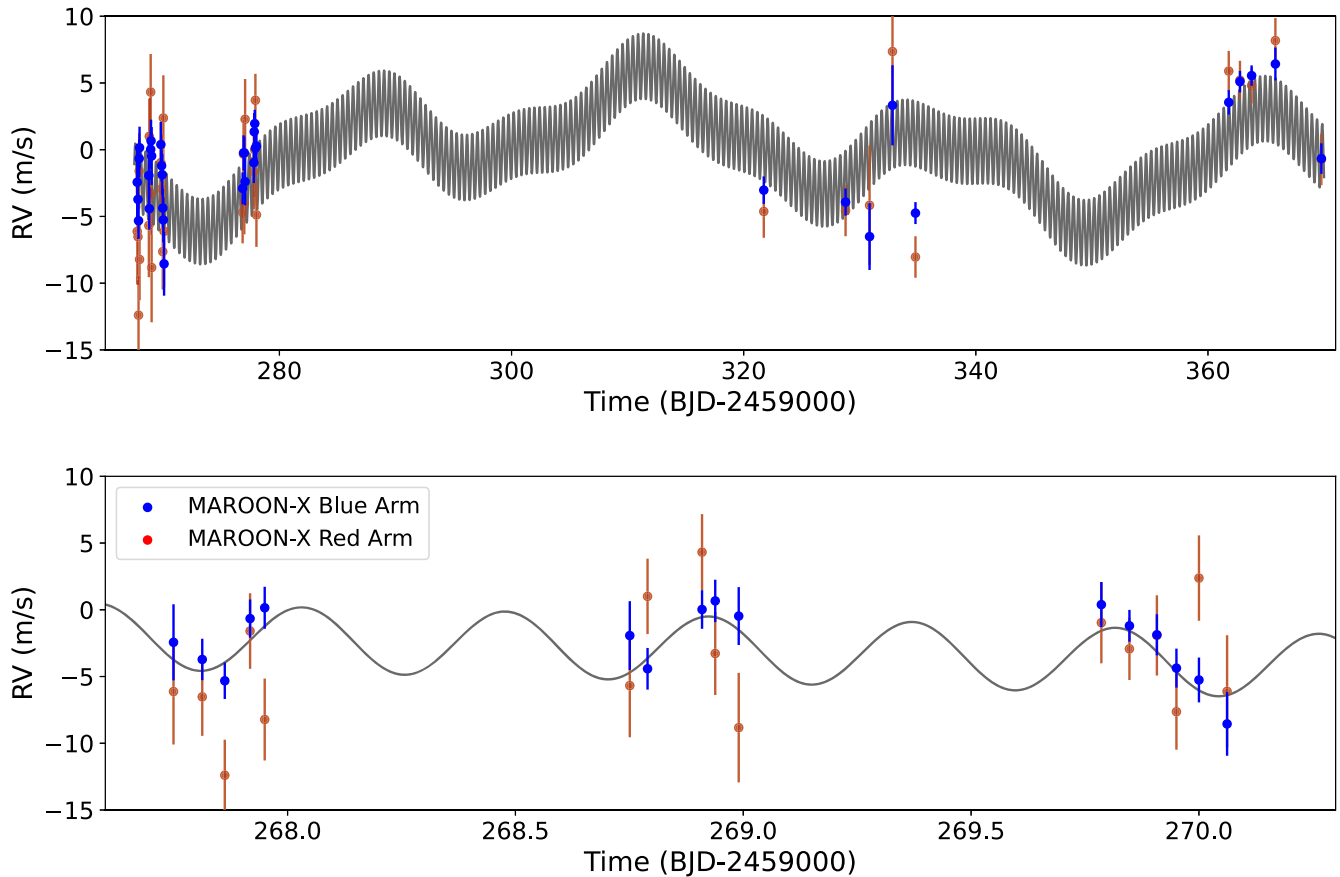
Figure 2. Top: the MAROON-X RVs collected from 2021 February to May over three different runs (red-arm RVs shown in red, blue-arm RVs shown in blue). The gray line is the best-fit Keplerian orbital model for all four planets in the TOI-561 system. Bottom: RVs from our highest-cadence run in 2021 February, highlighting the fully sampled orbit of TOI-561 b.

between parameters (no strong covariances or degeneracies were found).

Our entire RV data set is shown in Figure 3 with our best-fit model consisting of all four planets. The phase-folded best-fit models for each planet are shown in Figure 4. We computed the mass for each planet using the best-fit semiamplitudes, stellar mass from Weiss et al. (2021), and planet orbital periods (Table 4). Using the masses and radii measured here, we also computed the bulk density of each planet (Table 5).

For the USP TOI-561 b, the posterior of our fit yields a mass of $M_b = 2.24 \pm 0.20\,M_\oplus$. This is 1.2σ below the previously published value from Weiss et al. (2021) using observations solely from HIRES and 1.8σ above the initial value published by Lacedelli et al. (2021) using observations solely from HARPS-N. It is in agreement within 1σ of the updated mass by Lacedelli et al. (2022), which utilized both HIRES (60) and HARPS-N (144) RVs.

We also measured the mass of TOI-561 b using just the blue-arm RVs from MAROON-X during our February high-cadence run to highlight the unique abilities of MAROON-X. Using these 16 RVs, we measured a planet mass of $M_b = 2.7 \pm 0.48$ $M_\oplus$. MAROON-X was able to achieve a 17% fractional uncertainty with 16 RVs, compared to a fractional uncertainty of 35% using 80 measurements with HIRES. The value agrees with the mass derived using all three spectrographs and is closer to the new best-fit mass than the initial published values using only HIRES or HARPS-N. The combination of HARPS-N, HIRES, and MAROON-X data allowed us to measure the

mass of TOI-561 b with a fractional uncertainty of 9.6%, placing it among the most precisely known RV masses for planets with $R_p < 1.5\,R_\oplus$ (see Dai et al. 2019; Soto et al. 2021; Trifonov et al. 2021, for other examples).

Figure 5 shows our mass and radius measurements for all four TOI-561 planets in the context of those from the broader sub-Neptune-sized exoplanet population. We measured the density of TOI-561 b as $\rho_b = 4.8 \pm 0.5\,\mathrm{g\,cm^{-3}}$. This density places TOI-561 b as one of the lowest-density planets with $R_p < 1.5\,R_\oplus$.[26] We also show the mass–radius and density–radius curves for planets of three different compositions that span the possible range for solid rocky planets: iron-only, Earth-like ($\sim$30% iron), and iron-free silicate rock (Zeng et al. 2019). Our measurements for the mass and radius of TOI-561 b place it less than 1σ below the curve for an iron-free silicate rock planet. This means that while TOI-561 b appears to be low density for a super-Earth-sized planet, it is consistent both with solutions that include a gaseous envelope and with those that require none.

4. Error Budget

If TOI-561 b has a gaseous envelope, it would be one of the only planets in the "rocky" planet regime ($R < 1.5\,R_\oplus$) to host one (Kipping et al. 2014; Almenara et al. 2018). Before we proceed to composition modeling based on these mass and

---

[26] For perspective, a planet with an Earth-like composition at 1.37 $R_\oplus$ would have a density of 6.8 g cm^{-3}.

Table 4
Radvel Model Parameters for the Keplerian Orbit of the TOI-561 System

		Parameter	Unit	Median Posterior Value	Prior
TOI-561 b		P	Days	0.4465688	Fixed
		T_c	BJD	2,458,686.30	
		e		0	
		K	m s^{-1}	2.18 ± 0.20	Uniform
TOI-561c		P	Days	10.778831	Fixed
		T_c	BJD	2,458,527.06	
		e		0	
		K	m s^{-1}	2.22 ± 0.23	Uniform
TOI-561d		P	Days	25.7126	Fixed
		T_c	BJD	2,458,521.88	
		e		0	
		K	m s^{-1}	3.04 ± 0.25	Uniform
TOI-561e		P	Days	77.1437	Fixed
		T_c	BJD	2,458,538.18	
		e		0	
		K	m s^{-1}	2.36 ± 0.23	Uniform
HIRES		σ	m s^{-1}	2.8 ± 0.3	Hardbound 0,10
		γ	m s^{-1}	-1.7 ± 0.3	Uniform
HARPS-N		σ	m s^{-1}	2.0 ± 0.2	Hardbound 0,10
		γ	m s^{-1}	-0.004 ± 0.20	Uniform
MAROON-X Blue	February	σ	m s^{-1}	0.40 ± 0.3	Hardbound 0,10
		γ	m s^{-1}	-2.4 ± 0.4	Uniform
	April	σ	m s^{-1}	1.6 ± 0.9	Hardbound 0,10
		γ	m s^{-1}	-1.7 ± 1.1	Uniform
	May	σ	m s^{-1}	1.7 ± 0.8	Hardbound 0,10
		γ	m s^{-1}	-1.8 ± 0.93	Uniform
MAROON-X Red	February	σ	m s^{-1}	2.74 ± 0.95	Hardbound 0,10
		γ	m s^{-1}	-3.63 ± 0.83	Uniform
	April	σ	m s^{-1}	3.67 ± 1.82	Hardbound 0,10
		γ	m s^{-1}	-2.50 ± 1.22	Uniform
	May	σ	m s^{-1}	0.44 ± 1.25	Hardbound 0,10
		γ	m s^{-1}	-1.06 ± 0.95	Uniform 0,10

Note. The period and conjunction time are taken from Table 1 and are more precise than we would be able to determine using RVs; therefore, we fixed them in our analysis. Jitter (σ) and RV offset (γ) for each instrument are also listed, with unique jitter and offsets allowed for each run with MAROON-X.

radius measurements, it is important to examine the uncertainties that restrict our ability to determine a precise density.

Our ability to characterize any exoplanet is limited by our ability to characterize its host star, as our measurements for the mass and radius of TOI-561 b are determined relative to the mass and radius of TOI-561. Estimates of stellar radius usually come from the Stefan–Boltzmann law,

$$L_\odot = 4\pi R_\odot^2 \sigma_{\rm SB} T_{\rm eff}^4, \tag{1}$$

where $L_\odot$ is the luminosity, $R_\odot$ is the radius, $\sigma_{\rm SB}$ is the Stefan–Boltzmann constant, and $T_{\rm eff}$ is the effective temperature of the
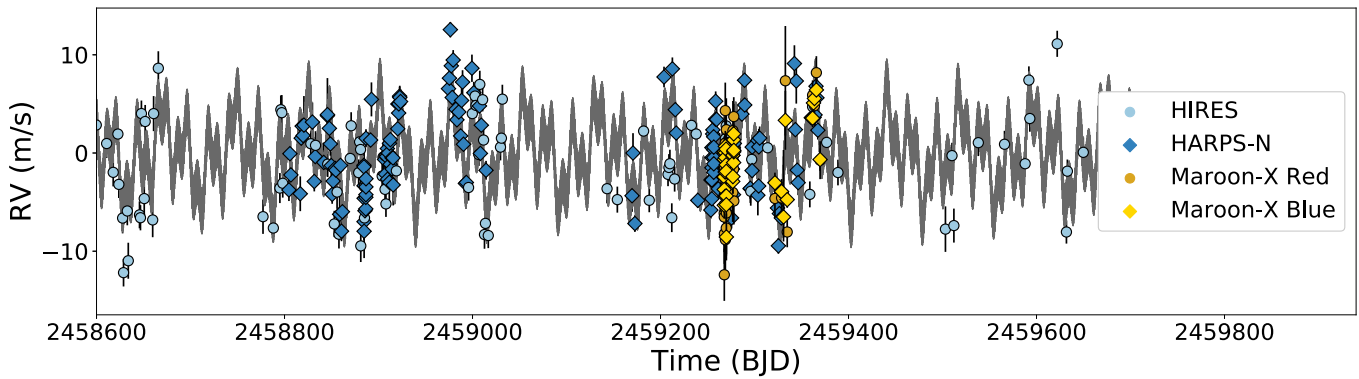
Figure 3. RV vs. time of TOI-561 measured with HIRES, HARPS-North, and MAROON-X (both red and blue arms), with 1σ error bars. The gray line represents our best-fit four-planet Keplerian orbital model.

star. Measuring the luminosity of a star requires the distance to the star, along with bolometric flux. Assigning an uncertainty to bolometric flux involves propagating the uncertainties in atmospheric model grids, photometric zero-points, and reddening corrections. As a result, Tayar et al. (2022) suggest a noise floor of $\sim$2% for measuring bolometric fluxes and therefore luminosities. Effective temperatures of stars are defined through bolometric flux and angular diameter and serve as fundamental calibrators for model-dependent methods such as high-resolution spectroscopy. This places a precision floor of $\sim$2% on effective temperature. Overall, Tayar et al. (2022) recommend a noise floor of $\sim$4% in stellar radius and $\sim$5% in stellar mass.

Angular diameter, bolometric flux, and effective temperature of stars are model parameters in the infrared flux method (IRFM; Blackwell et al. 1980) or SED fitting (Stassun et al. 2017), which can then be used to infer stellar radii. Additionally, isochrone modeling can be used to infer the stellar radius (along with mass, density, and age) using measurements of effective temperature, metallicity, surface gravity, and parallax in conjunction with 3D dust maps (Choi et al. 2016; Huber et al. 2017).

Figure 6 shows the range of values for the mass and radius of TOI-561 across different publications and methods, along with their published uncertainties. Lacedelli et al. (2021) use isochrones to measure stellar mass and radius, Lacedelli et al. (2022) use the IRFM to determine a stellar radius, and Weiss et al. (2021) use both SED fitting and isochrone grid modeling. None of the values include systematic uncertainties to account for intrinsic uncertainties in measuring bolometric flux or effective temperature, and all four of these measurements fall above the 4% precision floor from Tayar et al. (2022). The scatter in stellar radius among all of the values in Figure 6 is $\sim$4.5%, and the scatter of the four values discussed above is $\sim$3%, which is in agreement with the Tayar et al. (2022) prediction for method-dependent scatter.

To investigate the effects of these differences on planet composition, we constructed two sets of stellar parameters using the most conservative and the most optimistic cases. For the conservative case we use the isochrone radius and mass from Weiss et al. (2021) but inflate the uncertainty in radius from 2.6% to 4%. For the optimistic case we use the mass and radius from Lacedelli et al. (2022), with the 0.6% uncertainty on the radius as published. Figure 7 shows the 2D mass and radius distributions of TOI-561 b found using the conservative

cases. We drew 10,000 samples of stellar mass and stellar radius from Gaussian distributions centered on the published values (although using the inflated 1σ error bars for our conservative case).[27] For each trial, we drew the transit depth and semiamplitude from Gaussian distributions centered on the values measured in this work from Table 5. We used these values to calculate the planet mass and radius in each trial, and we recovered what fraction of our trials are consistent with a rocky planet solution and do not require a gaseous envelope or water layer. We deemed a planet as being consistent with a rocky planet composition if it falls below (i.e., more dense than) the "pure rock" composition line in Figure 7 (Zeng et al. 2019).

In the most conservative case (4% errors in stellar radius, using the isochrone-derived radius from Weiss et al. 2021), we find that the mass and radius of TOI-561 b are consistent with a gas-free rocky composition $\sim$40% of the time (Figure 7), while the optimistic case ($<$1% error in stellar radius) produces rocky planets only 21% of the time. Therefore, our measurements for planet mass and radius of TOI-561 b indicate that the planet is potentially too low in density to have a rocky composition— however, this claim only holds with 1σ significance with the most optimistic choice of stellar parameters, and less than 1σ significance with a more conservative choice of stellar parameter uncertainties.

The parameters that contribute most to the uncertainty in planet composition are the transit depth and semiamplitude, followed by the choice of stellar radius (4%; Figure 6). For the transit depth and semiamplitude, additional measurements would help to shrink this uncertainty and would help determine the nature of this planet's composition. Meanwhile, our ability to precisely and accurately determine stellar radii will remain a limiting factor in our ability to characterize TOI-561 b.

5. Planet Composition

Given the uncertainty in planet parameters, we cannot determine whether TOI-561 b is a rocky planet or has a gaseous envelope. We can, however, investigate the range of possible

---

[27] Stellar mass and radius are not independently varying parameters, so we tested the sensitivity of our results on the strength of the stellar mass–radius covariance. We drew parameters from Gaussian distributions for stellar mass and radius assuming no covariance, and we also drew assuming 100% covariance and found no significant effect ($\sim$1% variation) in the final results due to the relatively larger uncertainties on semiamplitude and transit depth. To ensure that our errors are conservative wherever possible, we assume no covariance in values reported.
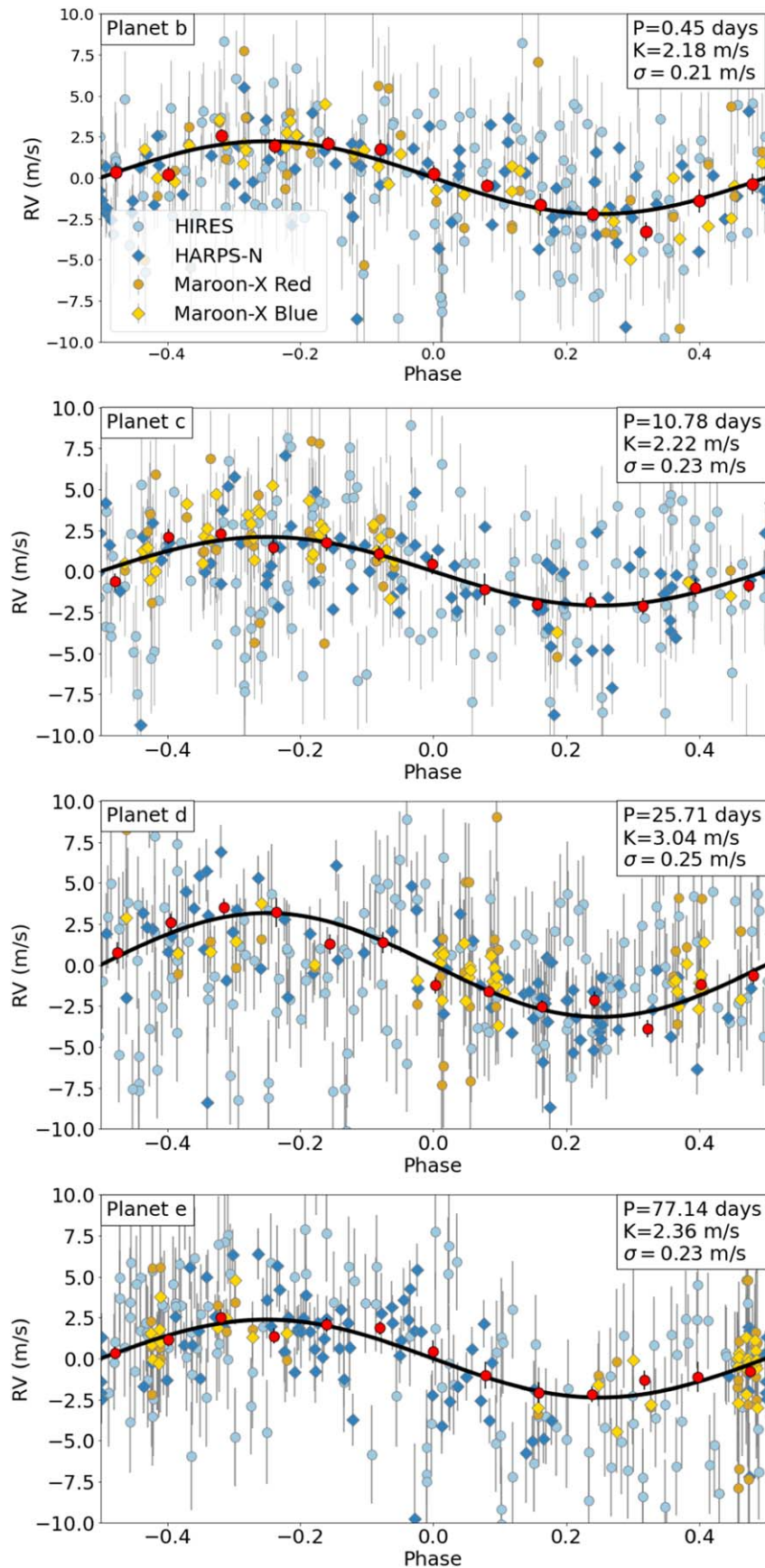
Figure 4. Top panel: the RVs phase-folded at the period of TOI-561 b, after subtracting the RV components from the other three planets based on our best-fit model. The model RV curve for planet b is overplotted in black, with the model period, semiamplitude (K), and standard deviation in semiamplitude (σ) shown. The phase-folded weighted mean RVs and their uncertainties are shown in red. Middle and bottom panels: same as the top panel, but for planets c, d, and e.
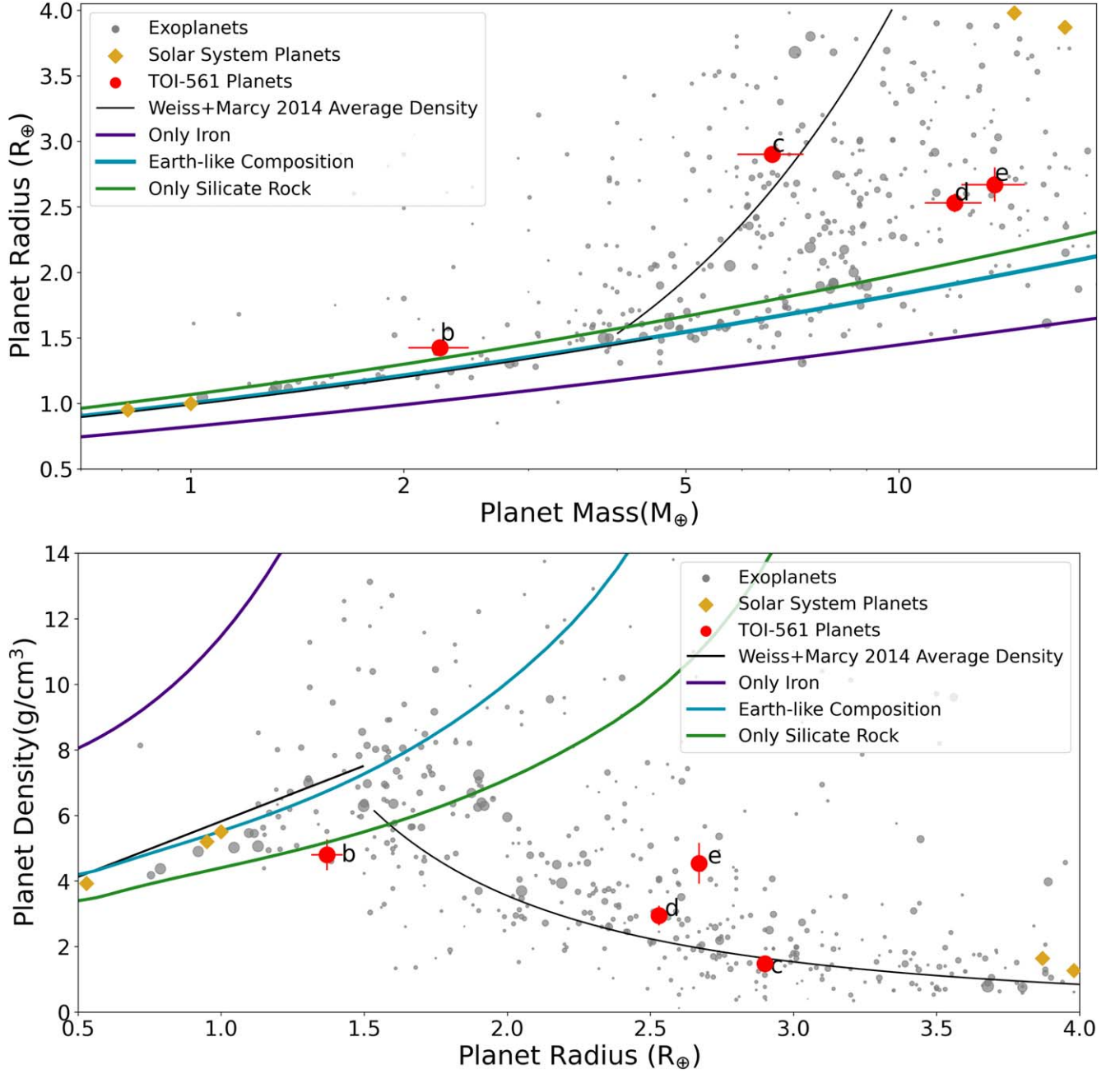
Figure 5. Planet mass (top panel) and density (bottom panel) as a function of radius for all known exoplanets with radii $R < 4\ R_\oplus$ that have RV-determined mass measurements with fractional uncertainties <100% (gray points). The sizes of the points (excluding TOI-561 system planets) scale inversely with the fractional uncertainty of their mass measurement. The masses and densities for the planets orbiting TOI-561 are shown with their 1σ uncertainties (red points). The empirical mass–radius and density–radius relations from Weiss & Marcy (2014) are shown as black lines. The mass–radius and density–radius curves for planets of solid iron, solid rock, and an Earth-like composition from Zeng et al. (2019) are shown (colored lines).

Table 5
Directly Modeled and Derived Parameters Based on Our MCMC Analysis of the Four Transiting Planets in TOI-561

Planet Name	b	c	d	e
Period, P (days)	0.4465688 ± 0.0000008	10.778831 ± 0.000036	25.7124 ± 0.0002	77.03 ± 0.25
Semimajor axis, a (au)	0.0106 ± 0.0004	0.089 ± 0.003	0.159 ± 0.006	0.33 ± 0.01
Radius, R ($R_\oplus$)	1.37 ± 0.04	2.91 ± 0.04	2.82 ± 0.07	2.55 ± 0.13
Semiamplitude, K (m s^{-1})	2.18 ± 0.20	2.22 ± 0.23	3.04 ± 0.25	2.36 ± 0.23
Mass, M ($M_\oplus$)	2.24 ± 0.20	6.6 ± 0.73	12.15 ± 1.10	13.6 ± 1.4
Density, ρ (g cm^{-3})	4.8 ± 0.5	1.46 ± 0.19	2.81 ± 0.33	4.91 ± 0.74

Note. The stellar mass (0.805 $M_\odot$) and radius (0.832 $R_\odot$) used to compute planet mass and radii are isochrone values from Weiss et al. (2021).
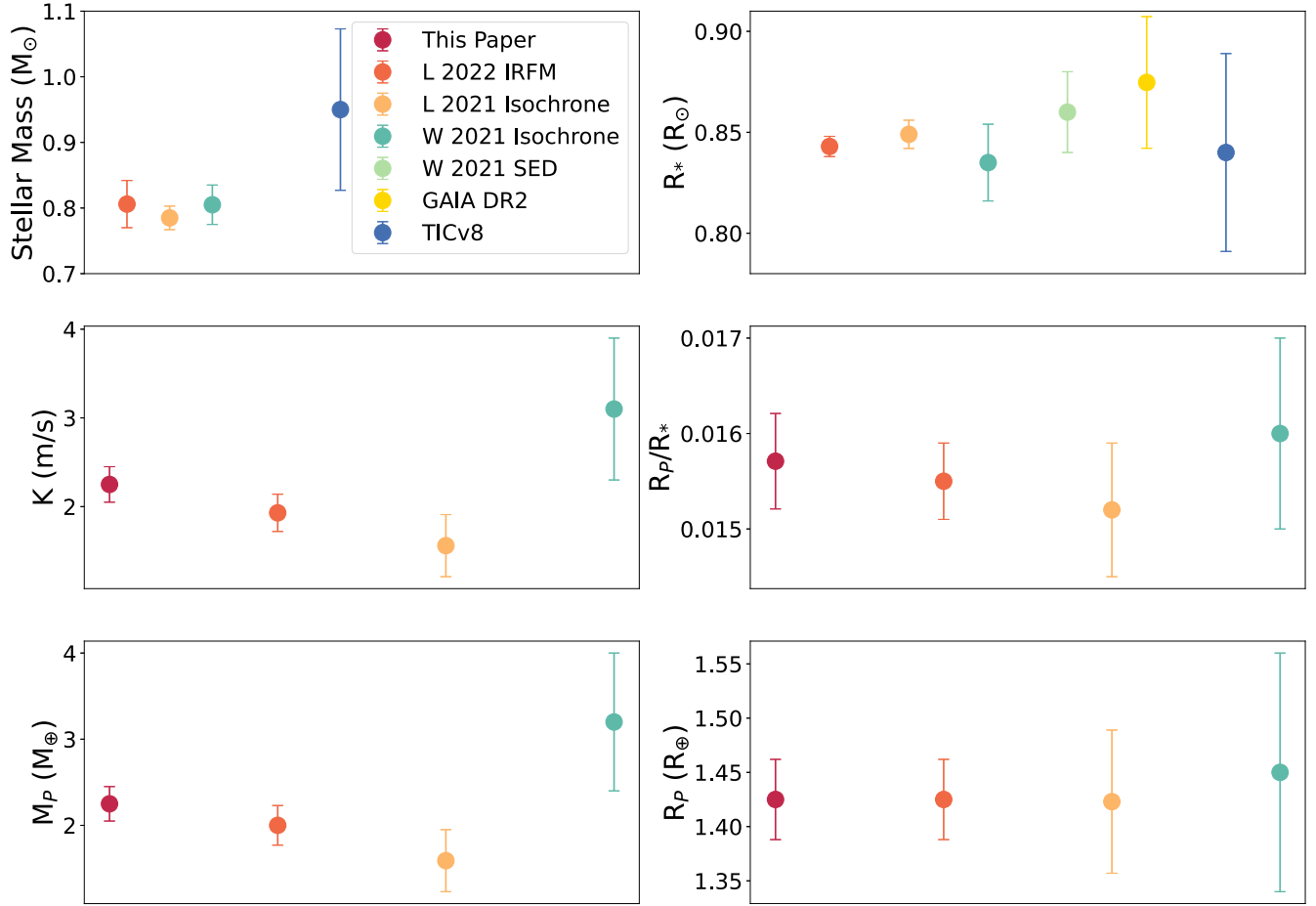
Figure 6. All available published values for the stellar mass and radius of TOI-561, along with semiamplitude (K), R_p/R_*, planet mass (M_P), and planet radius (R_P) for TOI-561 b, are shown with their 1σ uncertainties. The values for stellar radius and mass shown here are found using the IRFM, SED fitting, or isochrone grid modeling. Legend key: L 2022 = Lacedelli et al. (2022); L 2021 = Lacedelli et al. (2021); W 2021 = Weiss et al. (2021).

solid compositions given our planet mass measurement and identify at what solid radius TOI-561 b would mirror the iron/rock-building abundances present in the host star. We can investigate the effects of high melt fraction for the mantle, and we briefly discuss possible envelope compositions.

Assuming negligible ice, water, or volatile fractions, we can express solid planet compositions in terms of the fraction of iron to total planet mass, or core mass fraction (CMF). For this section, we adopt the stellar parameters found using isochrone models from Weiss et al. (2021), with errors inflated to 4% in stellar radius and 5% in stellar mass, and the RV semiamplitude and R_P/R_* listed in Table 5. We performed interior modeling using BurnMan 0.9 (Cottaar et al. 2016), which takes user-provided equations of state and the masses of individual layers in a differentiated planet and computes the inner and outer radii of each layer. We incorporated BurnMan in an iterative scheme that estimates the mass of a planet with a given radius and specified mass distributions between the different layers (in this case, a solid metallic inner core, a liquid metallic outer core, and a silicate mantle comprising $MgSiO_3$ [bridgmanite]). Burnman does not incorporate atmospheric modeling, so our models account only for the solid portion of the planet. For a complete discussion on composition modeling using Burn-Man, see Brinkman et al. (2022, in review).

We also used SuperEarth to model the interior of TOI-561 b (Valencia et al. 2006, 2007). Like BurnMan, SuperEarth divides planets into three primary layers (an iron core, rocky

mantle, and ice/water layer), but instead of pure $MgSiO_3$, SuperEarth uses a more nuanced mantle composition with four layers. The upper mantle includes olivene ($MgSiO_4$) and pyroxene; the transition zone features wadsleyite, ringwoodite, and pyroxene; the lower mantle includes bridgmanite and magnesiowustite; and the lower-most mantle has the same composition as the lower mantle but features a high-pressure bridgmanite (post-perovskite). In addition, SuperEarth takes user-provided mole fractions of silica inclusion in the iron core (here assumed to be 0), as well as iron mole fractions in the mantle (here assumed to be 0.1). A more thorough description of SuperEarth can be found in Plotnykov & Valencia (2020).

One source of uncertainty in our composition modeling is the degree to which the solid interior of TOI-561 b is differentiated. We assumed that the planet is differentiated, a consequence of energy released and melting occurring during accretion (Chao et al. 2021). However, the mass–radius relation of rocky planets is not very sensitive to their degree of differentiation (Elkins-Tanton & Seager 2008), with an expected difference of ~2.5% in radius—smaller than our uncertainty on the radius itself (Plotnykov & Valencia 2020).

To explore the range of possible compositions, we built planets that vary in composition from 0% iron core (CMF = 0) to 100% iron (CMF = 1.0) with a mass of 2.24 $M_\oplus$ and allow the radius to vary. This not only allows us to see what rocky planet compositions are possible within 1, 2, and 3 standard deviations from our measured radius but also allows us to see
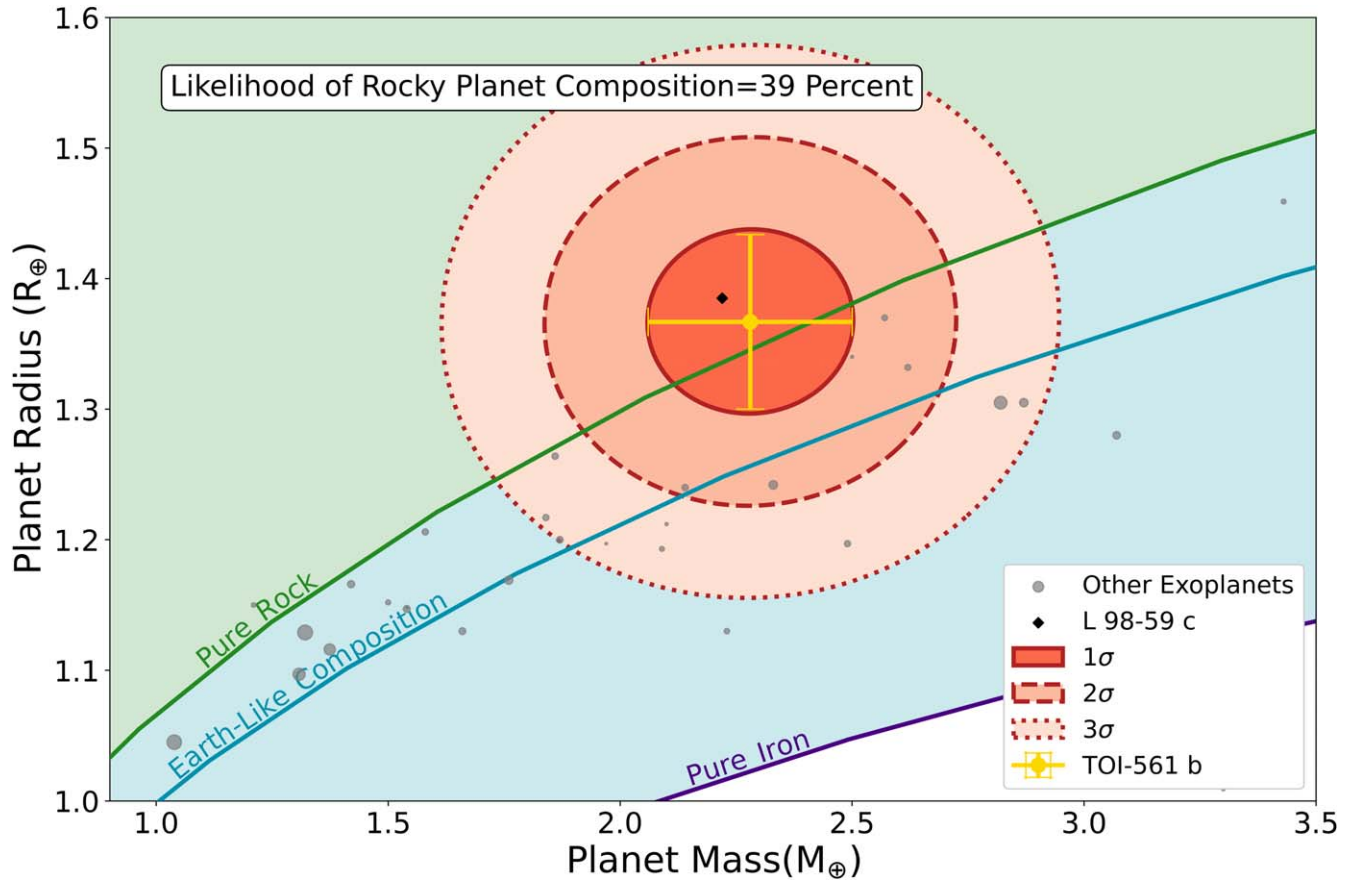
Figure 7. The mass and radius of TOI-561 b and uncertainties (1σ, 2σ, and 3σ contour regions) based on our new measurements (Table 5). We used stellar parameters from Weiss et al. (2021) and inflate the uncertainties on mass and radius to match the error floors established in Tayar et al. (2022) (4% in radius, 5% in mass). The mass and radius of TOI-561 b are consistent with a rocky composition—a bulk composition containing only silicate rock and iron (blue shaded region)—in 40% of trials and are consistent with a planet that needs a gaseous envelope (green shaded region) in 60% of trials. The population of known exoplanets with radius $R < 1.6$ $R_\oplus$ that have mass measurements is shown for context, and the size of the points (excluding TOI-561 b) scales inversely with the fractional uncertainty of their mass measurement. L98-59 c is highlighted as a recently characterized super-Earth with mass and radius measurements similar to those of TOI-561 b.
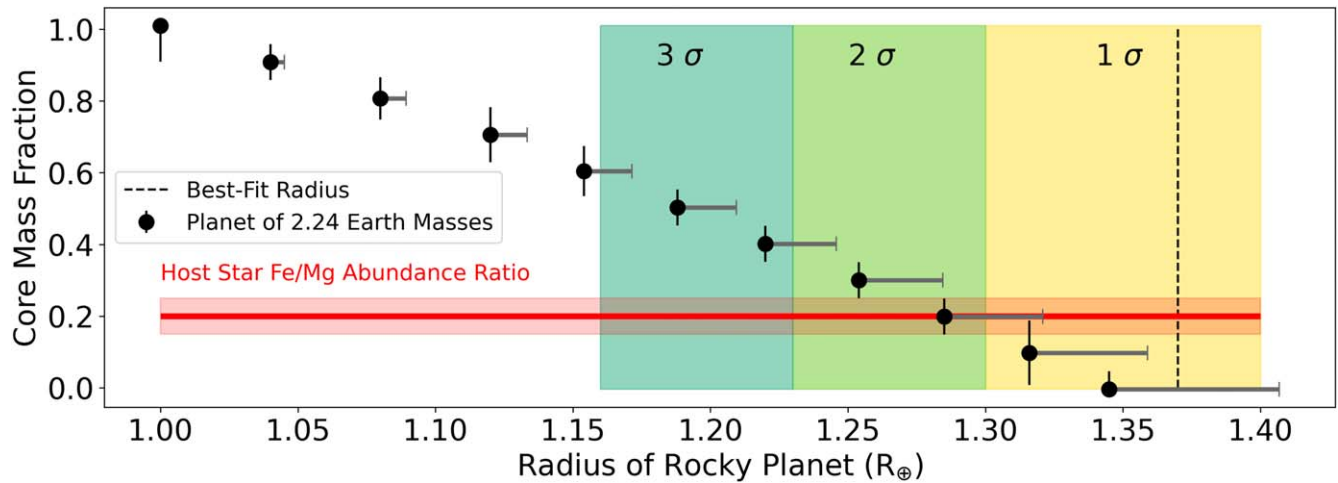
Figure 8. Here we show the range of possible compositions for the interior, rocky portion of TOI-561 b that are consistent within 1, 2, and 3 standard deviations of our measured planet radius and mass. We use SuperEarth to simulate planets at varying radii, with varying fractions of iron and silicate rock that are expressed as the fraction of iron core mass to the total planet mass, also called CMF. The uncertainties in CMF represent the spread in compositions that produce a planet within 1σ of the measured mass. The gray upper bound uncertainty in radius (gray) represents a ~5% increase in rocky mantle depth that the planet would experience given a melt fraction in the mantle of 0.5 (Bower et al. 2019), inflating the total radius of the planet. The host star has an abundance ratio of iron/(iron+rock-building elements) of 0.22, and this composition line lies at the 1σ bound for the radius of TOI-561 b.

the full range of interior solid compositions of various radii that could be present under a gaseous envelope. Our results using SuperEarth are shown in Figure 8, but we note that the

planet radii across all possible compositions held at fixed mass generated by BurnMan and SuperEarth differ by only ~1%.

The smallest possible planet that produces a mass consistent with our mass measurement (although it does not match the radius measurement) is a core made of 100% iron, corresponding to a CMF of 1.0 at 1 $R_\oplus$. An iron core of this size would require a thick gaseous envelope to match the measured planet radius.[28] The largest possible planet, made of 100% silicate rock corresponding to a CMF of 0, would have a radius of 1.35 $R_\oplus$. The best-fit radius (1.37 $R_\oplus$) is larger than that of the largest solid rocky planet (CMF = 0 planet) but is within 1σ of it. Thus, our mass and radius measurements favor a silicate-rich, iron-poor planet (low CMF) if we assume that the planet has no gas envelope, although the presence of a gas envelope would be consistent with any of the CMFs we tested.

Melt fraction is another critical factor to consider in assessing the composition of TOI-561 b. The equilibrium temperature of the planet ($\sim$2300 K) indicates that a significant portion of the rocky mantle might be molten, which could increase the depth of the rocky mantle by up to 10% for a melt fraction of 1.0 (Bower et al. 2019). Without heat redistribution from an atmosphere,[29] we would expect a melt fraction of <0.5, but this could still produce up to a 5% increase in rocky mantle depth, which would increase the total radius of the planet. Upper limits on radius size given a melt fraction of 0.5 are shown in gray on Figure 8. In the scenario in which TOI-561 b has a melt fraction close to 0.5, planet compositions with CMF = 0, 0.1, and 0.2 are all consistent with our measured radius to within 1σ.

5.1. Host Star Composition

The host star TOI-561 has abundance measurements for silicon ([Si/H] = -0.24 ± 0.05 dex), magnesium ([Mg/H] = -0.20 ± 0.05 dex), and iron ([Fe/H] = -0.41 ± 0.05 dex) (Weiss et al. 2021), which allows us to compare Fe/Mg and Fe/Si ratios in the star to the expected CMF of the planet given the protostellar nebular composition of the system.

Using solar abundances from Lodders (2019), we find the absolute abundances (rather than relative to solar) of Mg, Si, and Fe in TOI-561. We then use the atomic weight of each species (55.8 u for Fe, 24.3 u for Mg, 28 u for Si) to calculate the mass of each species relative to hydrogen. This gives us mass ratios of Fe/Si = 1.25 ± 0.29 and Fe/Mg = 1.18 ± 0.27.

Using the mantle mineral composition modeled using `SuperEarth`, we can recover the expected mass ratio of Fe/Si and Fe/Mg given a specified CMF. A mass ratio of Fe/Si = 1.25 ± 0.29 gives a CMF = 0.22 ± 0.05. We find that a mass ratio of Fe/Mg = 1.18 ± 0.27 is consistent with a CMF = 0.20 ± 0.05. Magnesium is less volatile than silicon and is thought to be better preserved through planet formation; therefore, Fe/Mg is thought to be a better proxy for the prestellar nebula (Yakovlev et al. 2018). We have plotted the Fe/Mg derived CMF of 0.2 as the host star composition in Figure 8, but note that a CMF of either 0.20 or 0.22 for TOI-561 b produces a planet that is consistent to within 1σ of our

mass and radius measurements, assuming that the rocky mantle has a high melt fraction.

The mass and radius of TOI-561 b are very similar to those of L98-59 c (Demangeon et al. 2021), as seen in Figure 7. L98-59 c is also a super-Earth-sized planet with mass and radius measurements that suggest that it might be too low in density for a solid rocky composition, but those measurements are also consistent with a rocky composition to within 1σ. It is particularly interesting that while L98-59 is an M dwarf and TOI-561 is an early K dwarf, they are both metal-poor ([Fe/H] = -0.46 ± 0.26 dex and -0.41 ± 0.05 dex, respectively). While further measurements are needed to measure the composition of either planet with a high degree of confidence, both of these systems are consistent with the hypothesis that metal-poor prestellar nebulae tend to form metal-poor rocky planets (Brewer et al. 2018).

5.2. Possible Envelope Compositions

While we cannot yet determine whether TOI-561 b has an optically thick gaseous envelope, we can investigate some possible envelope compositions. Hydrogen–helium (H/He) atmospheres are thought to be the most common atmospheric composition for gaseous planets (Kite et al. 2020; Bean et al. 2021). The measured masses and radii of exoplanets with radii between $1 < R_\oplus < 4$ suggest that planets above 1.5 $R_\oplus$ host these H/He envelopes (mini-Neptunes) while planets below 1.5 $R_\oplus$ do not (super-Earths; Weiss & Marcy 2014; Fulton et al. 2017). Many of the planets that are currently smaller than 1.5 $R_\oplus$ and have periods of less than 10 days are thought to have previously had H/He atmospheres during planet formation, like their mini-Neptune cousins, which they subsequently lost (Owen & Wu 2017; Gupta & Schlichting 2019). There are two stages during planet formation when this loss of atmosphere can occur: spontaneous mass loss following the dispersal of the planet-forming disk (Ginzburg et al. 2018), or, if the atmosphere is retained through disk dispersal, through subsequent core-powered mass loss (Gupta & Schlichting 2019) and/or photoevaporation (Owen & Wu 2017).

In the case of spontaneous mass loss, the pressure surrounding the planet suddenly drops when the disk disperses, leaving little to tie H/He envelopes to their host planet aside from gravity. Ginzburg et al. (2016) give a criterion under which a planet will retain a H/He-dominated atmosphere during disk dispersal:

$$\frac{M_c}{M_\oplus} > 6.3 \left(\frac{T_{\text{eq}}}{10^3 \, \text{K}} \right)^{4/3}, \tag{2}$$

where M_c is the mass of the rocky core of the planet and T_{eq} is the planet equilibrium temperature. For both sub-Neptunes and super-Earths, the majority of the planet's mass is contained within the rocky core (Lopez & Fortney 2014), giving $M_c = 2.2 \, M_\oplus$ for TOI-561 b. With an Earth-like albedo, TOI-561 b would have an equilibrium temperature $T_{\text{eq}} = 2300$ K. Under these conditions, TOI-561 b does not meet this criterion and would likely lose a H/He envelope spontaneously during disk dispersal. Letting albedo vary, we find that for any albedo <0.9995 TOI-561 b is too hot to retain an atmosphere through spontaneous mass loss. Given that the highest-albedo object in the solar system is Enceladus at $\alpha = 0.81$ (Howett

---

[28] Note that Earth's atmosphere, which is one-millionth of its mass, is optically thin and does not contribute to Earth's apparent radius, unlike the gaseous envelopes we consider.
[29] We have no way with current measurements of knowing whether TOI-561 b has either an optically thin atmosphere or an optically thick envelope made of high mean molecular weight species. The melt fraction could therefore be larger than 0.5, which would put the radius of a planet with CMF = 0.2 even closer to the measured radius of TOI-561 b.

et al. 2010), it is highly unlikely that TOI-561 b has managed to retain a primordial H/He envelope.

Several alternatives to H/He, particularly those with high mean molecular weight, are possible candidates for a gaseous envelope surrounding TOI-561 b. Lacedelli et al. (2022) suggest a liquid water layer or a water steam envelope. This scenario becomes more likely if the escape efficiency of H_2O atmospheres is much lower than for H_2-dominated atmospheres (Yoshida et al. 2022), or if very large quantities of H_2O are produced by oxidation of hydrogen by liquid magma (Kite & Schaefer 2021).

Another species worth considering is CO_2. The escape efficiency for a pure-CO_2 atmosphere has been argued to be very low (Tian 2009), so retaining a pure-CO_2 atmosphere would be easier than retaining the same mass of H_2O. However, even with low escape efficiency, the initial CO_2 content needed would be greater than the (fractional) CO_2 content of Earth and Venus (Tian 2009; Kite & Barnett 2020). Chondritic carbon values (carbon primarily in rock form as opposed to gaseous) for TOI-561 b would lead to a ∼1500 km (17% of total planet radius) $CO_2/CO+0.5O_2$ atmosphere in equilibrium with a magma ocean and would be enough to explain its radius even when invoking an Earth-like interior (B. Peng & D. Valencia 2023, in preparation).

TOI-561 b is in also in the temperature regime where we would expect silicate rock to begin vaporizing (Kite et al. 2016), so a thin envelope could be produced from the evaporation of the rocky mantle. A silicate vapor atmosphere might be detectable in the future through SiO absorption/emission (Zilinskas et al. 2022).

6. Conclusion

We collected 70 RVs using MAROON-X on Gemini and 42 RVs using HIRES on Keck I to improve the mass measurement of the USP super-Earth planet TOI-561 b. We combined our new RVs with literature RVs, literature photometry, and two new sectors of TESS photometery to characterize the planet. Our main conclusions are as follows:

1. We measure a mass of $M_b = 2.24 \pm 0.20\, M_\oplus$, a radius of $R_b = 1.37 \pm 0.04\ R_\oplus$, and a density of $\rho_b = 4.8 \pm 0.5\, \mathrm{g\,cm^{-3}}$ for TOI-561 b. The mass, radius, and densities of all four planets in the TOI-561 system can be found in Table 5.

2. While the low density of TOI-561 b suggests that it might host a volatile envelope, it is consistent with an iron-poor rocky composition. Further, our measurements show that TOI-561 b is consistent within 1σ of being a rocky planet with a CMF of 0.2—matching the Fe/Si and Fe/Mg abundance ratios in its host star. TOI-561 b is consistent with the hypothesis that stars tend to form planets reflective of their abundance ratios.

3. If this planet indeed hosts a gas envelope, it is likely composed of high mean molecular weight species, differentiating it from the H/He envelopes that are typical of sub-Neptune-sized planets. Envelope composition possibilities include those dominated by water or carbon dioxide, as well as evaporated silicates from the highly irradiated mantle.

4. The largest sources of uncertainty on the density of TOI-561 b are the transit depth and RV semiamplitude, followed by choice in stellar radius from literature values.

We assessed the probability of TOI-561 b requiring a gaseous envelope by sampling the 2D uncertainty space in planet mass and radius, and we find that the probability ranges from 60% to 80% depending on the choice of stellar parameters.

TOI-561 b has the potential to be a rocky planet whose composition reflects the iron and rock-building element abundances in its host star—a common product of planet formation. It also has the potential to be a very unusual super-Earth hosting a high mean molecular weight envelope, potentially even made of evaporated rock. Until a more precise transit depth and a more accurate host star radius are determined, the interior and atmospheric composition of TOI-561 b will be difficult to constrain. Future observations with JWST may help us determine the presence of an atmosphere or gaseous envelope by measuring the day/night temperature differential and allowing us to infer heat transport across the surface of the planet.

Facilities: Transiting Exoplanet Survey Satellite (TESS), W. M. Keck Observatory, Gemini Observatory.

Software: Exoplanet (Foreman-Mackey et al. 2021), Batman (Kreidberg 2015), Lightcurve (Lightkurve Collaboration et al. 2018), RadVel (Fulton et al. 2018), emcee (Foreman-Mackey et al. 2013), BurnMan 0.9 (Cottaar et al. 2016), SuperEarth (Valencia et al. 2007; Plotnykov & Valencia 2020) NumPy (Harris et al. 2020), Matplotlib (Hunter 2007), pandas (Wes 2010), Astropy (Astropy Collaboration et al. 2013; Astropy Collaboration, et al. 2018; Astropy Collaboration et al. 2022), SciPy (Virtanen et al. 2020).

ORCID iDs

Casey L. Brinkman ⓘ https://orcid.org/0000-0002-4480-310X
Lauren M. Weiss ⓘ https://orcid.org/0000-0002-3725-3058
Fei Dai ⓘ https://orcid.org/0000-0002-8958-0683
Daniel Huber ⓘ https://orcid.org/0000-0001-8832-4488
Edwin S. Kite ⓘ https://orcid.org/0000-0002-1426-1186
Diana Valencia ⓘ https://orcid.org/0000-0003-3993-4030
Jacob L. Bean ⓘ https://orcid.org/0000-0003-4733-6532
Corey Beard ⓘ https://orcid.org/0000-0001-7708-2364
Aida Behmard ⓘ https://orcid.org/0000-0003-0012-9093
Sarah Blunt ⓘ https://orcid.org/0000-0002-3199-2888
Madison Brady ⓘ https://orcid.org/0000-0003-2404-2427
Benjamin Fulton ⓘ https://orcid.org/0000-0003-3504-5316
Steven Giacalone ⓘ https://orcid.org/0000-0002-8965-3969
Andrew W. Howard ⓘ https://orcid.org/0000-0001-8638-0320
Howard Isaacson ⓘ https://orcid.org/0000-0002-0531-1073
David Kasper ⓘ https://orcid.org/0000-0003-0534-6388
Jack Lubin ⓘ https://orcid.org/0000-0001-8342-7736
Mason MacDougall ⓘ https://orcid.org/0000-0003-2562-9043
Joseph M. Akana Murphy ⓘ https://orcid.org/0000-0001-8898-8284
Mykhaylo Plotnykov ⓘ https://orcid.org/0000-0002-9479-2744
Alex S. Polanski ⓘ https://orcid.org/0000-0001-7047-8681
Malena Rice ⓘ https://orcid.org/0000-0002-7670-670X
Andreas Seifahrt ⓘ https://orcid.org/0000-0003-4526-3747
Guðmundur Stefánsson ⓘ https://orcid.org/0000-0001-7409-5688
Julian Stürmer ⓘ https://orcid.org/0000-0002-4410-4712

References

Adibekyan, V., Dorn, C., Sousa, S. G., et al. 2021, Sci, 374, 330
Agol, E., Luger, R., & Foreman-Mackey, D. 2020, AJ, 159, 123
Almenara, J. M., Díaz, R. F., Dorn, C., Bonfils, X., & Udry, S. 2018, MNRAS, 478, 460
Angelo, I., & Hu, R. 2017, AJ, 154, 232
Astropy Collaboration, Price-Whelan, A. M., Lim, P. L., et al. 2022, ApJ, 935, 167
Astropy Collaboration, Price-Whelan, A. M, Sipőcz, A. M., et al. 2018, AJ, 156, 123
Astropy Collaboration, Robitaille, T. P, Tollerud, E. J., et al. 2013, A&A, 558, A33
Bean, J., Seifahrt, A., Hartman, H., et al. 2010, Msngr, 140, 41
Bean, J. L., Raymond, S. N., & Owen, J. E. 2021, JGRE, 126, e06639
Blackwell, D. E., Petford, A. D., & Shallis, M. J. 1980, A&A, 82, 249
Bonomo, A. S., Zeng, L., Damasso, M., et al. 2019, NatAs, 3, 416
Bower, D. J., Kitzmann, D., Wolf, A. S., et al. 2019, A&A, 631, A103
Brewer, J. M., Wang, S., Fischer, D. A., & Foreman-Mackey, D. 2018, ApJL, 867, L3
Campante, T. L., Barclay, T., Swift, J. J., et al. 2015, ApJ, 799, 170

Chao, K.-H., deGraffenried, R., Lach, M., et al. 2021, ChEG, 81, 125735
Choi, J., Dotter, A., Conroy, C., et al. 2016, ApJ, 823, 102
Chontos, A., Akana Murphy, J. M., MacDougall, M. G., et al. 2021, AJ, 163, 297
Cottaar, S., Heister, T., Myhill, R., Rose, I., & Unterborn, C. 2016, GGG, 15, 833
Dai, F., Masuda, K., Winn, J. N., & Zeng, L. 2019, ApJ, 883, 79
Deck, K. M., Holman, M. J., Agol, E., et al. 2013, ApJL, 774, L15
Demangeon, O. D. S., Zapatero Osorio, M. R., Alibert, Y., et al. 2021, A&A, 653, A41
Dorn, C., Khan, A., Heng, K., et al. 2015, A&A, 577, A83
Dressing, C. D., Charbonneau, D., Dumusque, X., et al. 2015, ApJ, 800, 135
Elkins-Tanton, L. T., & Seager, S. 2008, ApJ, 688, 628
Eylen, V. V., Albrecht, S., Huang, X., et al. 2019, AJ, 157, 61
Foreman-Mackey, D., Hogg, D. W., Lang, D., & Goodman, J. 2013, PASP, 125, 306
Foreman-Mackey, D., Savel, A., Luger, R., et al. 2021, exoplanet-dev/exoplanet v0.5.1, Zenodo, doi:10.5281/zenodo.1998447
Fulton, B. J., Petigura, E. A., Blunt, S., & Sinukoff, E. 2018, PASP, 130, 044504
Fulton, B. J., Petigura, E. A., Howard, A. W., et al. 2017, AJ, 154, 109
Gan, T., Shporer, A., Livingston, J. H., et al. 2020, AJ, 159, 160
Ginzburg, S., Schlichting, H. E., & Sari, R. 2016, ApJ, 825, 29
Ginzburg, S., Schlichting, H. E., & Sari, R. 2018, MNRAS, 476, 759
Gupta, A., & Schlichting, H. E. 2019, MNRAS, 487, 24
Harris, C. R., Millman, K. J., van der Walt, S. J., et al. 2020, Natur, 585, 357
Howard, A. W, Johnson, J. A., Marcy, G. W., et al. 2010, ApJ, 721, 1467
Howett, C. J. A., Spencer, J. R., Pearl, J., & Segura, M. 2010, Icar, 206, 573
Huber, D., White, T. R., Metcalfe, T. S., et al. 2022, AJ, 163, 79
Huber, D., Zinn, J., Bojsen-Hansen, M., et al. 2017, ApJ, 844, 102
Hunter, J. D. 2007, CSE, 9, 90
Kipping, D. M. 2013, MNRAS, 435, 2152
Kipping, D. M., Nesvorný, D., Buchhave, L. A., et al. 2014, ApJ, 784, 28
Kite, E. S., & Barnett, M. N. 2020, PNAS, 117, 18264
Kite, E. S., Fegley, B. J., Schaefer, L., & Ford, E. B. 2020, ApJ, 891, 111
Kite, E. S., Fegley, B. J., Schaefer, L., & Gaidos, E. 2016, ApJ, 828, 80
Kite, E. S., & Schaefer, L. 2021, ApJL, 909, L22
Kreidberg, L. 2015, PASP, 127, 1161
Kumar, R., Carroll, C., Hartikainen, A., & Martin, O. A. 2019, JOSS, 4, 1143
Lacedelli, G., Malavolta, L., Borsato, L., et al. 2021, MNRAS, 501, 4148
Lacedelli, G., Wilson, T. G., Malavolta, L., et al. 2022, MNRAS, 511, 4551
Lightkurve Collaboration, Cardoso, J. V. d. M, Hedges, C., et al. 2018, Lightkurve: Kepler and TESS time series analysis in Python, Astrophysics Source Code Library, ascl:1812.013
Lodders, K. 2019, arXiv:1912.00844
Lopez, E. D., & Fortney, J. J. 2014, ApJ, 792, 1
Luger, R., Agol, E., Foreman-Mackey, D., et al. 2019, AJ, 157, 64
Marcy, G. W., & Butler, R. P. 1992, PASP, 104, 270
Marcy, G. W., Isaacson, H., Howard, A. W., et al. 2014, ApJS, 210, 20
Mills, S. M., Howard, A. W., Petigura, E. A., et al. 2019, AJ, 157, 198
Morton, T. D., Bryson, S. T., Coughlin, J. L., et al. 2016, ApJ, 822, 86
Newville, M., Stensitzki, T., Allen, D. B., & Ingargiola, A. 2014, LMFIT: Non-Linear Least-Square Minimization and Curve-Fitting for Python, v0.8.0, Zenodo, doi:10.5281/zenodo.11813
Owen, J. E., & Wu, Y. 2017, ApJ, 847, 29
Plotnykov, M., & Valencia, D. 2020, MNRAS, 499, 932
Rogers, L. A. 2015, ApJ, 801, 41
Salvatier, J., Wiecki, T. V., & Fonnesbeck, C. 2016, PeerJ Comp. Sci., 2, e55
Schulze, J. G., Wang, J., Johnson, J. A., et al. 2021, PSJ, 2, 113
Seager, S., & Mallén-Ornelas, G. 2003, ApJ, 585, 1038
Seifahrt, A., Bean, J. L., Stürmer, J., et al. 2016, Proc. SPIE, 9908, 990818
Seifahrt, A., Bean, J. L., Stürmer, J., et al. 2020, Proc. SPIE, 11447, 114471F
Seifahrt, A., Stürmer, J., Bean, J. L., & Schwab, C. 2018, Proc. SPIE, 10702, 107026D
Soto, M. G., Anglada-Escudé, G., Dreizler, S., et al. 2021, A&A, 649, A144
Stassun, K. G., Collins, K. A., & Gaudi, B. S. 2017, AJ, 153, 136
Tayar, J., Claytor, Z. R., Huber, D., & van Saders, J. 2022, ApJ, 927, 31
Theano Development Team 2016, arXiv:1605.02688
Tian, F. 2009, ApJ, 703, 905
Trifonov, T., Caballero, J. A., Morales, J. C., et al. 2021, Sci, 371, 1038
Valencia, D., O'Connell, R. J., & Sasselov, D. 2006, Icar, 181, 545
Valencia, D., Sasselov, D. D., & O'Connell, R. J. 2007, ApJ, 656, 545
Virtanen, P., Gommers, R., Oliphant, T. E., et al. 2020, NatMe, 17, 261
Vogt, S. S., Allen, S. L., Bigelow, B. C., et al. 1994, Proc. SPIE, 2198, 362
Weiss, L. M., Dai, F., Huber, D., et al. 2021, AJ, 161, 56

Weiss, L. M., & Marcy, G. W. 2014, ApJL, 783, L6

Wes, M. 2010, in Proc. of the 9th Python in Science Conf., ed. S. van der Walt (Austin, TX: SciPy), 56

Winters, J. G., Cloutier, R., Medina, A. A., et al. 2022, AJ, 163, 168

Yakovlev, O. I., Ryazantsev, K. M., & Shornikov, S. I. 2018, GeocI, 56, 71

Yee, S. W., Tamayo, D., Hadden, S., & Winn, J. N. 2021, AJ, 162, 55

Yoshida, T., Terada, N., Ikoma, M., & Kuramoto, K. 2022, ApJ, 934, 137

Zechmeister, M., Reiners, A., Amado, P. J., et al. 2018, A&A, 609, A12

Zeng, L., Jacobsen, S. B., Sasselov, D. D., et al. 2019, PNAS, 116, 9723

Zilinskas, M., van Buchem, C. P. A., Miguel, Y., et al. 2022, A&A, 661, A126